Journal of Alloys and Compounds 509 (2011) 2745–2752

Contents lists available at ScienceDirect

Journal of Alloys and Compounds

journal homepage: www.elsevier.com/locate/jallcom

Influence of europium oxide doping on the structural and optical properties of pulsed laser ablated barium tungstate thin films

N. Venugopalan Pillai [a], V.P. Mahadevan Pillai [a,*], R. Vinodkumar [a], I. Navas [a], V. Ganesan [b], Peter Koshy [c]

[a] Department of Optoelectronics, University of Kerala, Kariavattom, Trivandrum-695581, Kerala, India
[b] UGC – DAE CSR, Khandwa Road, Indore 452 017, Madhyapradesh, India
[c] Electron Microscopy Division, National Institute for Inter Disciplinary Sciences and Technology, Thiruvananthapuram, Kerala, India

ARTICLE INFO

Article history:
Received 30 July 2010
Accepted 11 November 2010
Available online 18 November 2010

Keywords:
Nanostructured barium tungstate thin films
Europium oxide
Pulsed laser deposition
Hall–Williamson plot
Micro-Raman
PL emission

ABSTRACT

Nanostructured Eu_2O_3 doped Barium tungstate ($BaWO_4$) crystallites are successfully synthesized using pulsed laser deposition (PLD) technique. The influence of different Eu_2O_3 doping concentrations (1,2,3 & 5 wt.%) on the structural, surface morphological and optical properties are systematically studied using XRD, micro-Raman, SEM, AFM, UV–vis and photoluminescence spectroscopy. All the films are polycrystalline with tetragonal scheelite structure. The vibrational analysis of the atoms in $BaWO_4$ is studied by micro-Raman spectra using factor group analysis. The surface morphological analysis by SEM and AFM reveals the presence of fine nanoparticles with distinct grain boundaries in all the films. The band gap energy variation in the Eu_2O_3 doped $BaWO_4$ films is in accordance with the variation of the sizes of nano particles in the films. The films with higher Eu^{3+} doping concentrations (≥2 wt.%) show a PL emission peak centered around 614 nm when excited at 394 nm which can be attributed to the $^5D_0 \rightarrow {}^7F_2$ (0–2) transition of Eu^{3+} ion.

1. Introduction

Scheelite-structured tungstates are renowned for their excellent optical, structural properties and potential applications in the fields of scintillant arithmometer, X-ray gain screen, luminescence, and displays. Tetragonal scheelite structured ceramic oxides like $BaWO_4$ and $CaWO_4$, either doped or substituted by rare-earth elements, are important optical materials. They have attracted much attention because of their practical applications such as laser host materials in quantum electronics and scintillators in medical devices [1–4]. Moreover, because the attenuation constant of $BaWO_4$ lies in the range from microseconds to nanoseconds, it is also a potential and especially essential material for designing all-solid state lasers that can emit radiation in a specific spectral region. Photoluminescence study of different crystalline metal oxide ceramics doped mainly with rare earth ions such as Eu^{3+}, Er^{3+}, Nd^{3+} etc., revealed a considerable potential of these materials in optoelectronic applications [5,6]. These compounds can be widely used as phosphors in cathode-ray tubes, field emission, vacuum fluorescent and electroluminescent displays as well as scintillators in X-ray and positron emission tomography [5–9]. The optical properties of trivalent rare-earth ions (RE^{3+}) in tungstate materials with scheelite structure have been widely investigated [10–13], especially due to their attractive third order nonlinear dielectric susceptibilities [14,15]. Diverse techniques have been developed to synthesize $BaWO_4$ crystallites such as polymeric precursor method, precipitation method, molten salt method, super molecule template method, micro-emulsion method etc. [16]. In the present paper, pulsed laser deposition technique is used to synthesize Eu_2O_3 doped $BaWO_4$ crystallites with good crystalline morphology. To the best of our knowledge, no such studies on pulsed laser ablated Eu_2O_3 doped $BaWO_4$ crystallites have ever been reported.

2. Experimental details

Eu_2O_3 (1,2,3 & 5 wt.%) doped $BaWO_4$ thin films are prepared using pulsed laser deposition (PLD) technique. The deposition of the films is performed inside a stainless steel vacuum chamber using a *Q*-switched Nd: YAG laser (Spectra Physics, Quanta – Ray INDI – series) with 200 mJ of laser energy from a frequency doubled 532 nm radiation having pulse width 7 ns and repetition frequency 10 Hz. The sintered pellet (having 11 mm diameter and 3 mm thickness) used for the laser ablation is prepared from commercially available $BaWO_4$ and europium oxide (Sigma Aldrich, purity 99.9%) powders. The deposition of the films is done using laser energy of 140 mJ for duration of 20 min on quartz substrates (fixed at an on-axis distance of 6 cm from the target). The target is rotated with constant speed of 33 rpm to avoid pitting of the target and

* Corresponding author. Tel.: +91 471 2308167.
E-mail addresses: vpmpillai9@gmail.com, vpmpillai9@rediffmail.com (V.P.M. Pillai).

0925-8388/$ – see front matter © 2010 Elsevier B.V. All rights reserved.
doi:10.1016/j.jallcom.2010.11.061

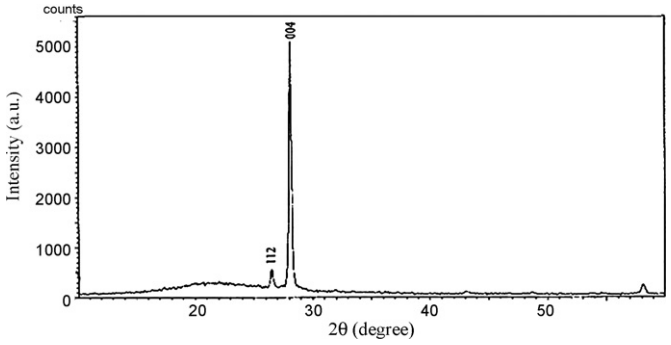

Fig. 1. The XRD pattern of undoped $BaWO_4$ film post-annealed at T_{ANN} = 800 °C.

to ensure uniform ablation. The ablated films are post-annealed at a temperature 800 °C for 4 h. The $BaWO_4$ films with different Eu^{3+} concentrations viz., 1%, 2%, 3% and 5% are designated as BWEu-1, BWEu-2, BWEu-3 and BWEu-5 respectively.

The crystalline structure and crystallographic orientation of annealed films are characterized by XRD measurements [XPERT PRO Diffractometer] using CuKα radiation of 0.15405 nm wavelength. Surface morphology and particle size distribution of the films are investigated by Scanning Electron Microscope [JEOL 5600]. The surface morphology at a nanometer scale is investigated using atomic force microscope (AFM) [Digital Instruments Nanoscope E, Si_3N_4 100 μ cantilever, 0.58 N/m force constant] measurements in contact mode. The rms surface roughness and grain size are obtained from a scan area of 5 μm × 5 μm. The thickness of the films is measured using a Dektak 6 M Stylus profiler. Micro Raman spectra of the films are recorded using Labram-HR 800 spectrometer equipped with excitation source having laser radiation at a wavelength of 488 nm from an argon ion laser. Optical transmission and reflectance spectra of the films are recorded using JASCO V 550 UV–vis–NIR double beam spectrophotometer in the region 190–900 nm. Room temperature photoluminescence spectra of the films are recorded at an excitation wavelength 394 nm using Horiba Jobin Yvon Flourolog 111 modular spectroflurometer equipped with a 450 W xenon lamp and Hamatsu R928-28 photomultiplier.

3. Results and discussion

3.1. XRD analysis

Figs. 1 and 2 show the GIXRD patterns of the undoped and Eu^{3+} doped $BaWO_4$ films annealed at T_{ANN} = 800 °C respectively. The undoped $BaWO_4$ film shows two peaks corresponding to (1 1 2) and (0 0 4) reflection planes of tetragonal scheelite with preferred orientation along ⟨0 0 4⟩ direction. Besides (1 1 2) and (0 0 4) reflection planes, all the doped films exhibit additional reflection planes corresponding to tetragonal scheelite structure of $BaWO_4$ (JCPDS Card no. 26-194) with preferred orientation in ⟨1 1 2⟩ direction. It is

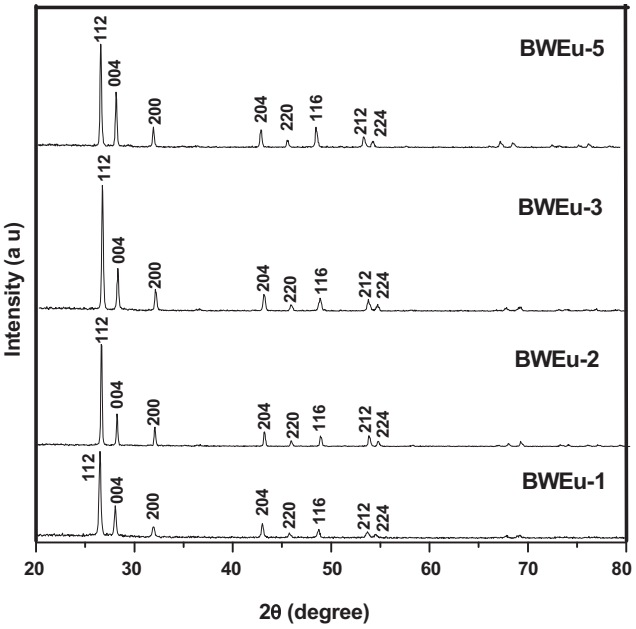

Fig. 2. The XRD patterns of Eu_2O_3 doped $BaWO_4$ films post-annealed at T_{ANN} = 800 °C.

observed that the intensity of the peaks from all planes enhances on increasing Eu_2O_3 doping concentration up to 3% and thereafter the intensity of XRD peaks decreases. This indicates that moderate doping of Eu_2O_3 (3 wt.%) increases the crystallinity and Eu_2O_3 doped film is more crystalline than other films. The absence of any Eu_2O_3 peaks in the XRD patterns of the films indicates that europium is well dissolved in $BaWO_4$ lattice. The lattice parameters of tetragonal scheelite system are calculated using the following equation.

$$\sin^2\ \theta_{hkl} = \left(\frac{\lambda^2}{4a^2}\right)(h^2 + k^2) + \left(\frac{\lambda^2}{4c^2}\right) l^2 \quad (1)$$

where a and c are the lattice constants and h, k and l are the Miller indices, λ the X-ray wavelength and θ_{hkl}, half the diffraction angle of the peak. For $BaWO_4$ in bulk form with tetragonal scheelite structure, the reported values of the lattice parameters a and c are 5.61 Å and 12.72 Å respectively and the unit cell volume V is 400 Å^3 [17]. The calculated values of the lattice parameters and unit cell volume (Table 1) are matching with the reported values, confirming the tetragonal scheelite phase in these films. The unit cell volume in the films decreases with increase in Eu_2O_3 doping concentration.

The average size of crystallites in the films is determined using the following Debye Scherrer's equation, [18]

$$D_{hkl} = \frac{0.9\ \ \lambda}{\beta_{hkl} \cos\ \ (\theta_{hkl})} \quad (2)$$

where λ is the X-ray wavelength, θ_{hkl} is the Bragg diffraction angle and β_{hkl} is the full width at half- maximum (FWHM) in radian of

Table 1
Lattice parameters, unit cell volume, particle size and micro strain of undoped and Eu_2O_3 doped $BaWO_4$ films.

Eu_2O_3 doping concentration (wt.%)	Thickness of the films (nm)	Lattice parameters		Unit cell volume (Å)^3	Crystallite size from Scherrer formula (nm)	Crystallite size from W–H plot (nm)	Lattice strain ($\times 10^{-3}$)
		a (Å)	c (Å)				
0	215	5.60	12.62	396	33	–	–
1	320	5.62	12.77	403.06	60	64	2.4
2	280	5.62	12.76	403.02	47	52	10.0
3	250	5.618	12.73	401.78	37	45	32.0
5	235	5.60	12.72	399.00	42	45	1.0

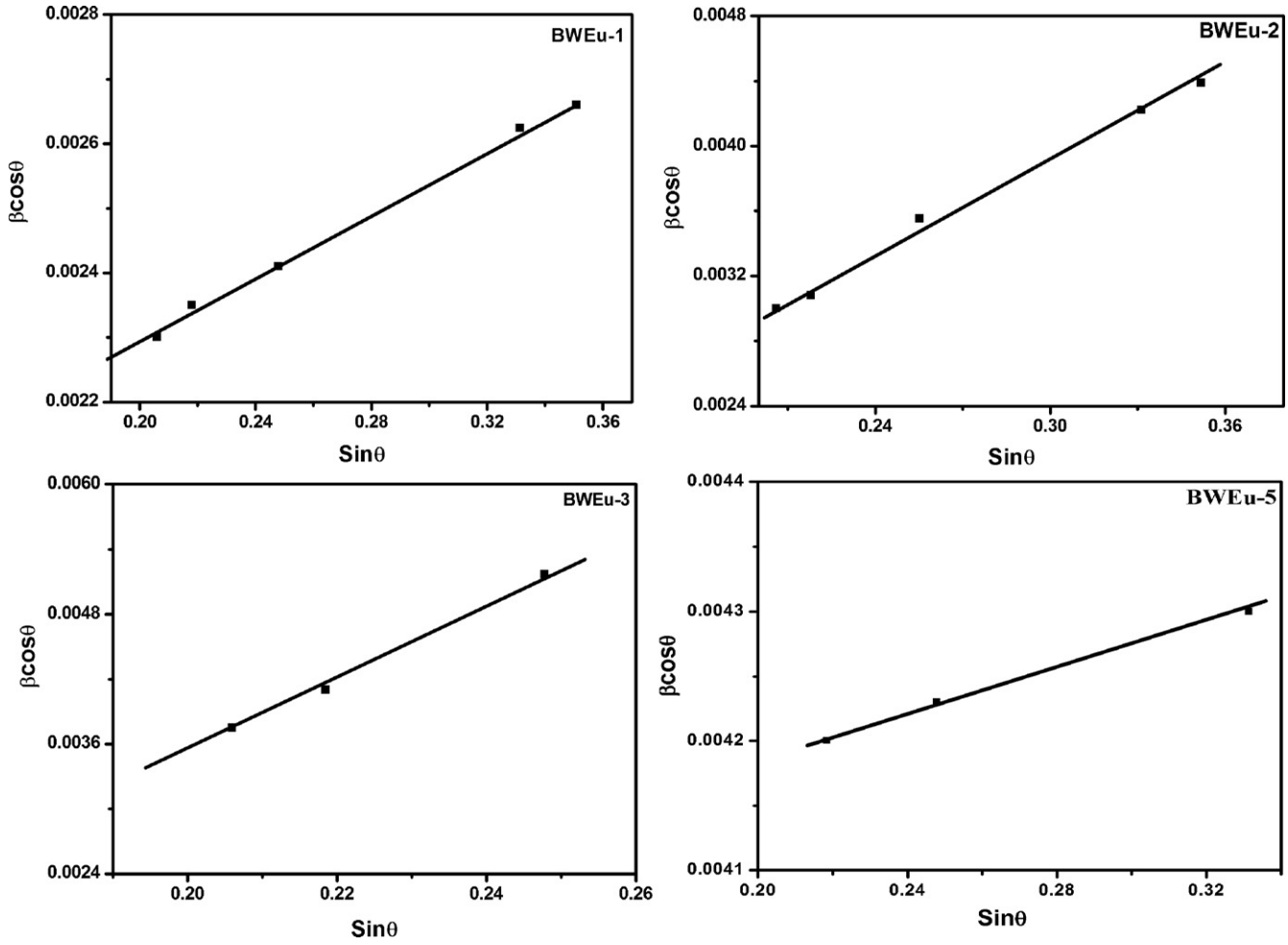

Fig. 3. Williamson–Hall plots of Eu_2O_3 doped $BaWO_4$ films post-annealed at 800 °C.

the main peak in the X-ray diffraction pattern. The particle sizes are found to be 33, 60, 47, 37 and 42 nm for the undoped, BWEu-1, BWEu-2, BWEu-3 and BWEu-5 films respectively, which confirm the presence of nanocrystallites in the films prepared in the present work. Thus the crystallite sizes of the films show definite variation with Eu_2O_3 doping concentration.

The internal stress, strain, lattice distortion or defects can broaden the XRD peaks, so that the mean size of the crystallites estimated using the Debye–Scherrer formula can be smaller than the actual value. The effect of crystallite size induced broadening and strain induced broadening in the full widths at half maximum (FWHM) of XRD peak can be studied using Williamson–Hall method [19]. The lattice strain and crystallite size are calculated from Willamson–Hall plots drawn by using the relation,

$$\beta \cos \theta = \frac{k\lambda}{D'} + 2\eta \sin \theta \quad (3)$$

where β is the FWHM of the XRD peak, θ is half the angle of diffraction corresponding to the peak, k is a constant which can be taken as 0.9, D′ is the size of the strain free crystallite and η is the lattice strain. The $\sin\theta$ vs. $\beta\cos\theta$ plot is a straight line whose intercept on the $\beta\cos\theta$ axis gives the value of $k\lambda/D'$ and its slope gives the lattice strain (Fig. 3). The calculated values of size of the crystallites and strain in the films are given in Table 1. The size of the crystallites calculated from Williamson–Hall plot differs appreciably from the corresponding values calculated from Debye–Scherrer equation and this indicates the presence of considerable lattice strain in the films.

3.2. Morphological analysis by SEM and AFM

Figs. 4 and 5 represents the SEM and AFM micrographs of Eu_2O_3 doped $BaWO_4$ films post-annealed at 800 °C. All the films exhibit the presence of fine nanoparticles with distinct grain boundaries. The SEM pictures of BWEu-1 and BWEu-5 films show agglomeration of grains forming clusters of different sizes. The BWEu-2 and BWEu-3 films show densely packed grains of different sizes with well-defined grain boundaries. The AFM images also present the same morphology as observed from the SEM macrographs. The AFM of BWEu-1 film displays non-uniform distribution of grains of different sizes whereas BWEu-2 film presents distribution of grains of bigger size with lot of porosity. The morphology of BWEu-3 film consists of a dense distribution of grains of smaller and bigger sizes. The AFM image of BWEu-5 film presents a dense distribution of grains with dominance of bigger grains. Thus the films with Eu_2O_3 doping concentration 2 and 3 wt.% show better surface morphology and grain distribution, compared to others. The root mean square surface roughness of the films is found using the WSxM software of Nanotec Electronica S.L. [20] and all the doped films show high values of rms surface roughness (Table 2).

3.3. UV–vis spectra

Fig. 6 represents the optical transmission spectra of undoped and Eu_2O_3 doped $BaWO_4$ films. The average optical transmittances of the films in the wavelength range 350–900 nm is calculated and are given in Table 2. The undoped film shows a very high transmit-

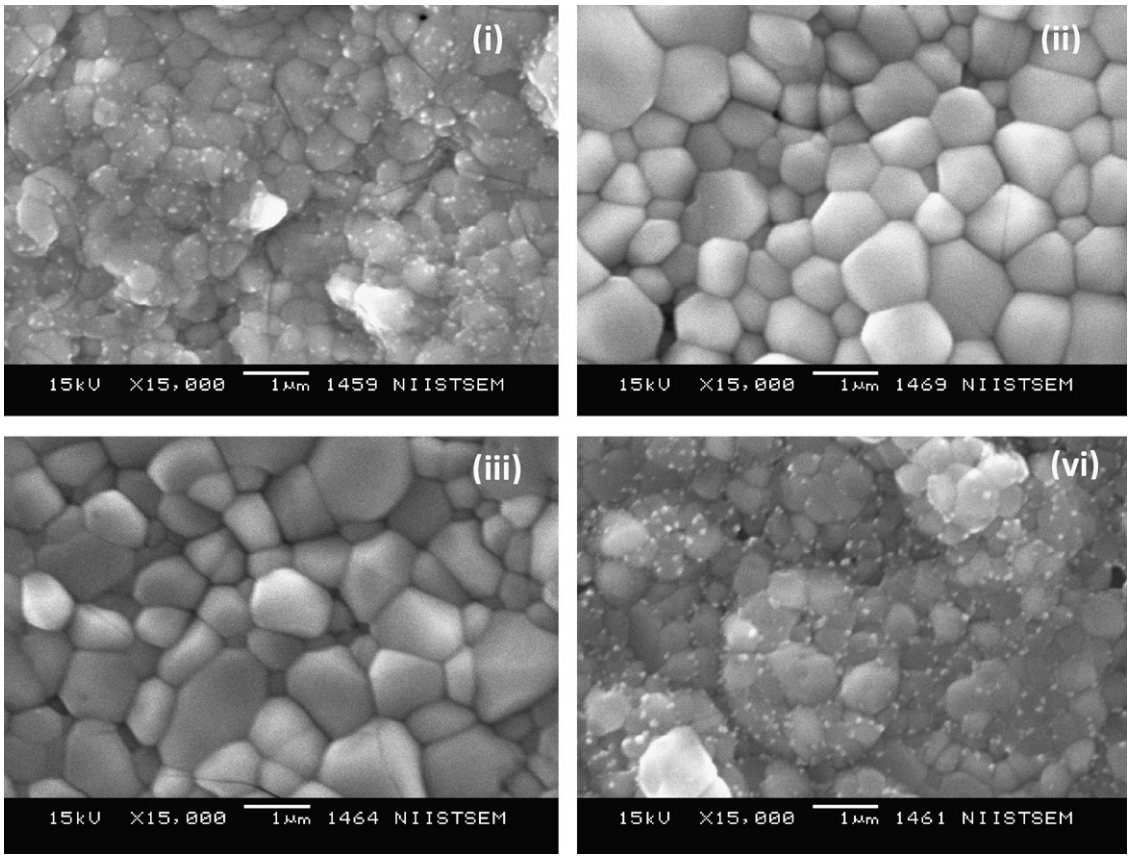

Fig. 4. The SEM images of Eu_2O_3 doped $BaWO_4$ films post-annealed at T_{ANN} = 800 °C (i) BWEu-1, (ii) BWEu-2, (iii) BWEu-3 and (iv) BWEu-5.

tance of ~82.5% whereas the doped films show only relatively lower values of transmittance. Among the Eu_2O_3 doped films, BWEu-3 shows the highest value for the optical transmittance (~58.3%). The XRD analysis shows that this film has the highest crystallinity compared to other films. The sharp decrease in the transmittance around the wavelength ~250 nm observed for all the films is due to the absorption edge of $BaWO_4$.

The transmittance spectral data obtained for the films are used to calculate the absorption coefficient, α at different wavelengths using the relation [21]

$$\alpha = \frac{\log \left[1/T\right]}{t} \quad (4)$$

where t is the thickness of the film and T is the transmittance of the film. For the parabolic band structure, the relation between the absorption coefficient (α) and the band gap energy E_g of the material can be estimated from the following relation [22,23]

$$(\alpha h\nu)^{1/n} = A(h\nu - E_g)^n \quad (5)$$

where A is band edge constant, ν is the transition frequency and the exponent n characterizes the nature of band transition. The values 1/2 and 3/2 for n correspond to direct allowed and direct forbidden transitions and 2 and 3 correspond to indirect allowed and indirect forbidden transitions respectively [24]. The band gap energy E_g can be obtained from extrapolation of the straight-line portion of the $(\alpha h\nu)^{1/n}$ vs. $h\nu$ plot to position $h\nu = 0$ (Tauc plot). The intercept on the $h\nu = 0$ axis directly gives the band gap energy E_g in eV. It is observed that for all the film, the best straight line is obtained for $n = 1/2$ which is expected for direct allowed transition. There are reports suggesting direct and indirect band gap nature for tungstates [25,26]. However, Lacomba-Perales et al. [27] have established the direct band gap nature for transitions in $BaWO_4$.

The band gap values are found to be 5.70, 5.23, 5.33, 5.66 and 5.62 eV (Table 2) for the un-doped and the BWEu-1, BWEu-2, BWEu-3 and BWEu-5 films respectively. For the undoped film, the size of the crystallite is 33 nm and it shows the highest optical band gap energy of 5.70 eV. Usually for the doped films, the band gap energy will be higher compared to the undoped films due to B–M shift. In the present case all the doped films show band gap energy lower than that of the undoped film and cannot be ascribed to B–M shift. The particle size calculation based on XRD analysis shows that all the doped films have crystallites whose size greater than that of the undoped film. BWEu-3 film

Table 2
Optical properties of undoped and Eu_2O_3 doped $BaWO_4$ films.

Eu_2O_3 doping concentration (wt.%)	Thickness of films (nm)	Root mean square surface roughness (nm)	Average optical transmittance in the range 350–900 nm (%)	Band gap energy (eV)
0	215	7	82.5	5.70
1	320	28	25.7	5.23
2	280	66	49.8	5.33
3	250	32	58.3	5.66
5	235	34	42.8	5.62

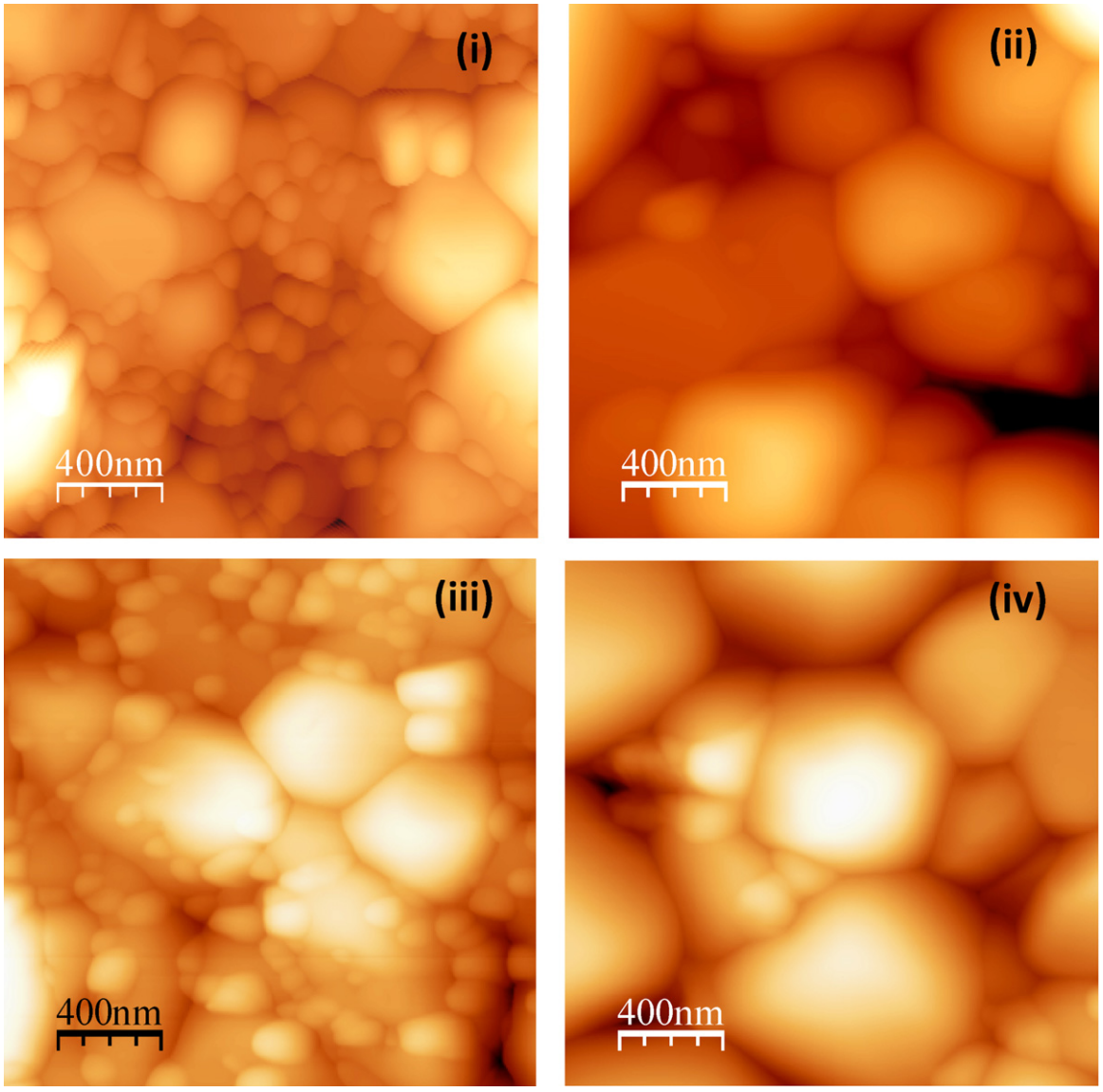

Fig. 5. The AFM images of Eu_2O_3 doped $BaWO_4$ films post-annealed at T_{ANN} = 800 °C, (i) BWEu-1, (ii) BWEu-2, (iii) BWEu-3 and (iv) BWEu-5.

Table 3
Correlation of intra-vibration of WO_4^{2-} ion in $BaWO_4$.

		Free ion Symmetry		Site Symmetry				Factor . group		
$f^{\gamma}=Z^B.\nu_{vib}$	ν_{vib}	T_d	correlation	S_4	C_ς	a_ς	correlation	C_{4h}	C_ς	a_ς
								Ag	1	2
2	1	A_1	→	A	1	2+2	→	Bg	1	3
								Eg	2	2
4	2	E	→	B	1	2+4	→	Au	1	3
								Bu	1	2
12	6	F_2	→	E	2	4	→	Eu	2	2

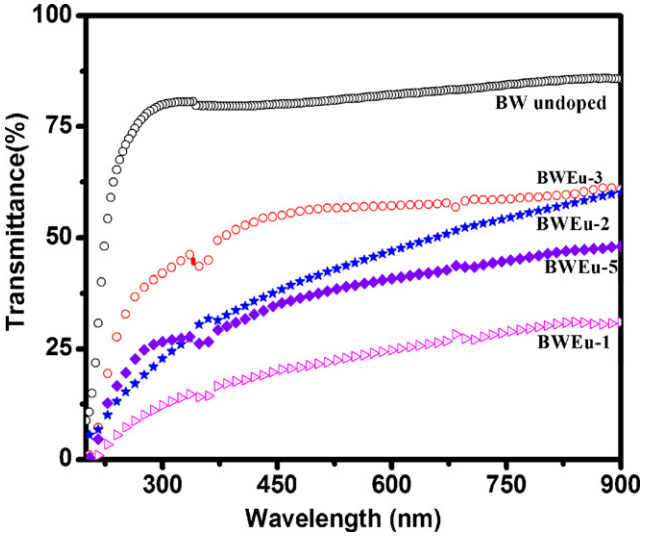

Fig. 6. Optical transmittance of laser ablated $BaWO_4$ films annealed at T_{ANN} = 800 °C as a function of Eu_2O_3 doping concentration.

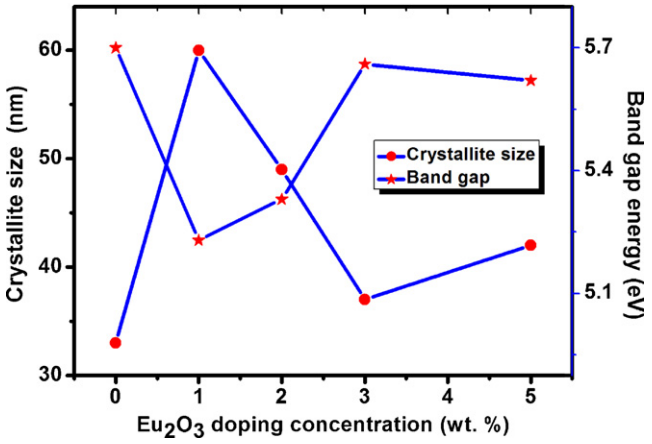

Fig. 7. Variation of Crystallite size and band gap energy of laser ablated $BaWO_4$ films as a function of Eu_2O_3 doping concentration.

having the lowest size of the crystallite (~37 nm) among the doped films possesses band gap energy 5.66 eV which is close to the value of band gap energy of the undoped film. BWEu-1 film having the highest size of the crystallite (~60 nm) possesses the lowest value of band gap energy 5.23 eV. It is expected that, as the particle size increases, band gap energy decreases due to quantum confinement. Thus the variations of the values of band gap energy in these films are in accordance with the variation of the size of the crystallites (Fig. 7).

3.4. Micro-Raman analysis

$BaWO_4$ crystallizes in tetragonal system with space group I41/*a* and factor group C_{4h} with two formula unit per Bravais cell. Two Ba atoms and two WO_4^{2-} ions occupy the S_4 site. Optical phonon modes of $BaWO_4$ crystal are calculated by correlation method developed by Fateley et al. [28]. Excluding the three acoustic modes, the 33 optical modes in $BaWO_4$ among the various factor group species are described as:

$$\Gamma^{\text{optical}} = 3A_g(\text{R}) + 5B_g(\text{R}) + 5E_g(\text{R}) + 4A_u(\text{IR}) + 3B_u + 4E_u(\text{IR}) \quad (6)$$

Out of these, A_g, B_g and E_g modes are Raman active and A_u and E_u modes are IR active where as B_u modes are inactive in

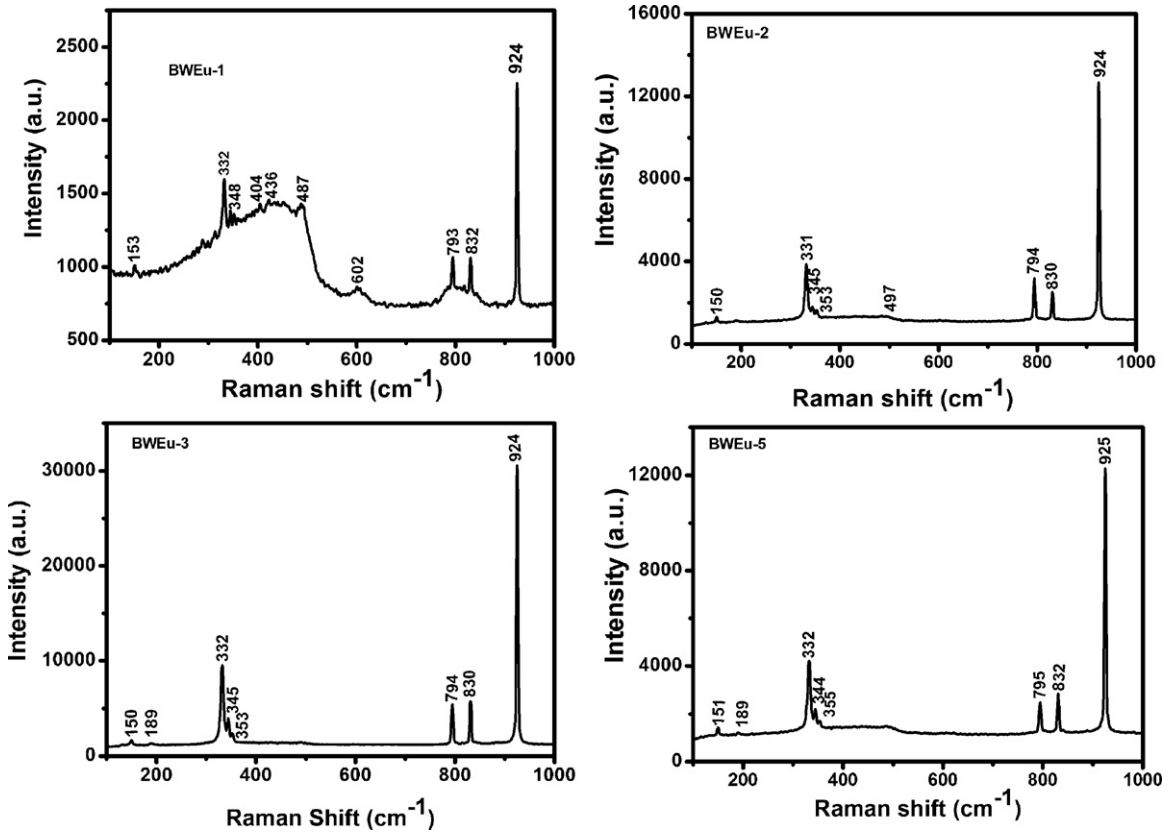

Fig. 8. Raman spectra of laser ablated Eu_2O_3 doped $BaWO_4$ films annealed at T_{ANN} = 800 °C.

Table 4
Micro-Raman spectral analysis of Eu_2O_3 doped $BaWO_4$ films.

Raman spectral data				
BWEu-1 (cm^{-1})	BWEu-2 (cm^{-1})	BWEu-3 (cm^{-1})	BWEu-5 (cm^{-1})	Assignments
				ν_1-WO_4^{2-}
924 v s	924 v s	924 v s	925 v s	
832 m	830 m	830 m	832 m	ν_3-WO_4^{2-}
793 m	794 m	794 m	795 m	
602 w, br	–	–	–	
497 w, br	497 w, br	–	–	
438 w, br				ν_4-WO_4^{2-}
404 w, br				
348 w	353 w	353 w	355 w	ν_2-WO_4^{2-}
332 m	345 m	343 m	344 w	
	331 s	332 s	332 s	
		189 w		
153 m	150 w	150 w	151 w	Lattice modes

vs – very strong, s – strong, m – medium, w – weak, br – broad.

both IR and Raman spectra. The distribution of internal modes of WO_4^{2-} ion is shown in Table 3. The correlation diagram for WO_4 ion (Table 3) maps out the site splitting and factor group splitting in the crystal.

Weinstock et al., have assigned the internal modes of WO_4^{2-} ion in aqueous solutions in the following way [29], the non-degenerate symmetric stretching mode ν_1 (A_1) ~ (931 ± 1) cm^{-1}, the doubly degenerate symmetric bending mode ν_2 (E) ~ (325 ± 2) cm^{-1} and the triply degenerate asymmetric stretching mode ν_3 (F_2) ~ (838 ± 4) cm^{-1}. They have not observed the ν_4 modes. But Liegeois-Duyckaerts et al. [30] assigned the triply degenerate asymmetric stretching mode ν_4 (F_3) around 353 cm^{-1}.

Fig. 8 represents the Raman spectra of Eu_2O_3 doped $BaWO_4$ films. Spectral data obtained for various films and their assignments are given in Table 4. The Raman bands in all films except BWEu-1 are sharp and intense whereas most of the Raman bands in the Raman spectrum of BWEu-1 are broad and less intense. This indicates that BWEu-1 film is less crystalline than other films. The most intense band observed in the Raman spectra of Eu_2O_3 doped $BaWO_4$ films around 924 cm^{-1} is assigned to non-degenerate stretching mode ν_1

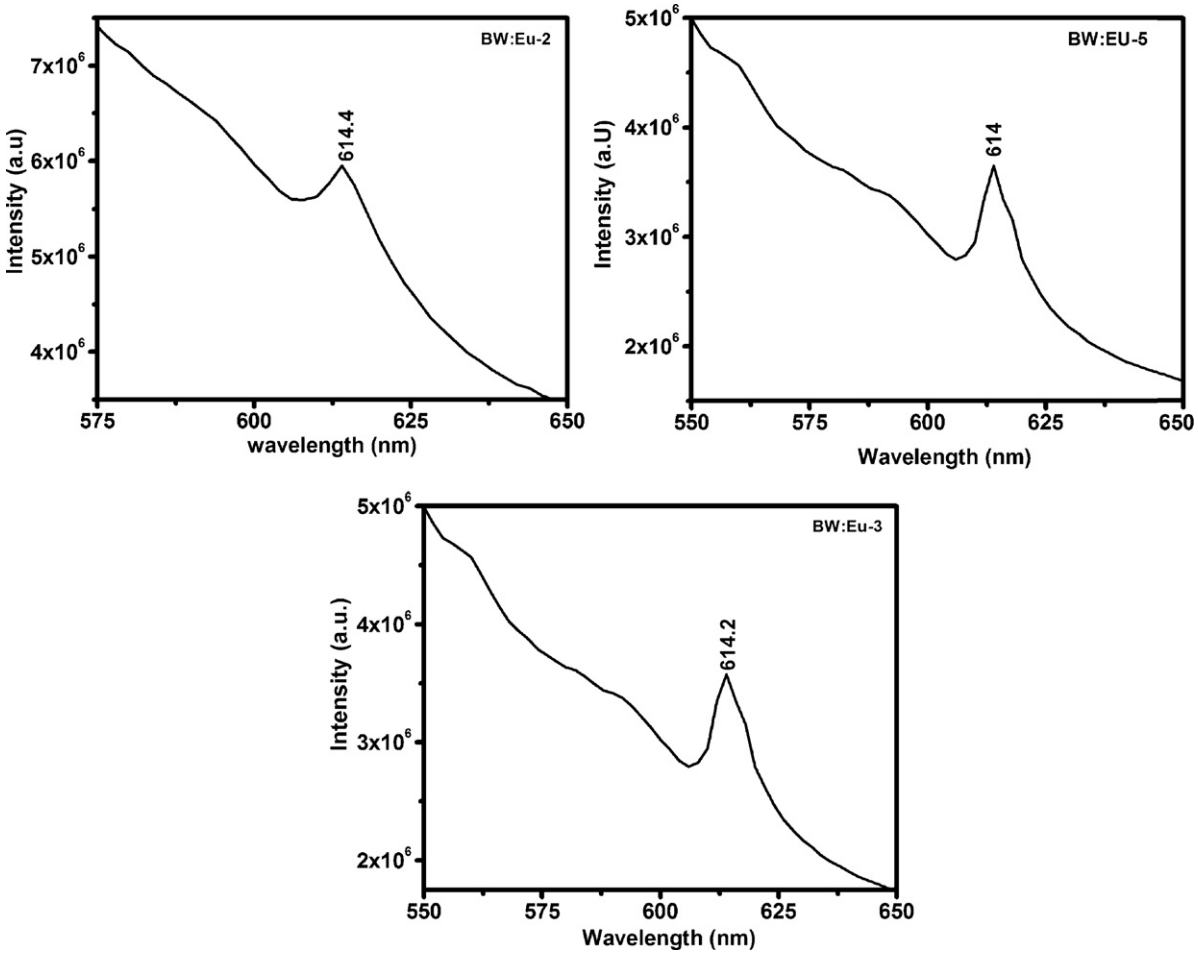

Fig. 9. PL emission spectra of Eu_2O_3 doped $BaWO_4$ films annealed at T_{ANN} = 800 °C.

(A_1) of WO_4^{2-} ion. The sharpness and intensity of the ν_1 mode can be an indication of the crystallinity of film. Among the Eu_2O_3 doped $BaWO_4$ films, BWEu-3 film shows the highest intensity for the ν_1 mode. This observation supports earlier inference drawn from the XRD data that BWEu-3 film is more crystalline than other films. The triply degenerate asymmetric stretching mode ν_3 (F_2) appears in the micro-Raman spectra of the films with partial lifting of degeneracy. This mode appears as two medium intense bands around 794 and 832 cm^{-1}. Apart from lifting the degeneracy, additional splitting has been observed for the doubly degenerate symmetric bending mode ν_2 (E) of WO_4^{2-} ion in the Raman spectra of all the films.

3.5. Photoluminescence (PL) studies

The PL emission of Eu^{3+}doped scheelite materials (AWO_4 type) mainly depend on excitation wavelength. These materials are known for their scintillating property i.e. they are able to convert energy of absorbed high energy photon or particle into a number of UV or visible photons [31]. When they act as host materials for Eu^{3+} ion, two emissions spectrum is possible for the samples that is, (i) when the excitation is fixed in the tungstate group (275–300 nm) and (ii) when the excitation is fixed directly in the Eu^{3+} ion (394 nm). Emission related to Eu^{3+} ions in these two cases are different. When excited by radiation of wavelength in the range 275–300 nm, Eu^{3+} ions give PL emission due to the transition $^5D_0 \rightarrow {}^7F_1$ (0–1) centered at 584 nm resulting from the high symmetric site occupancy of Eu^{3+} ion. When excited by radiation of wavelength 394 nm, the PL emission is due to the transition $^5D_0 \rightarrow {}^7F_2$ (0–2) transition centered at 614 nm due to occupation of Eu^{3+} ions in at least one site with low symmetry [31–33]. The PL intensity is larger in the second case compared to the first case. Fig. 9 shows the PL spectra of the Eu_2O_3 doped $BaWO_4$ films when excited with a radiation of wavelength 394 nm. The as-deposited and 1 wt.% Eu_2O_3 doped $BaWO_4$ films show no PL emission. But the films at higher Eu^{3+} doping concentrations show a PL emission peak centered around 614 nm and can be attributed to the $^5D_0 \rightarrow {}^7F_2$ (0–2) transition of Eu^{3+} ion as explained earlier. The intensity of the PL emission is found to be higher for 3 wt.% Eu_2O_3 doped $BaWO_4$ films.

4. Conclusion

The XRD patterns of the Eu_2O_3 doped $BaWO_4$ films show polycrystalline with tetragonal scheelite structure. In the undoped $BaWO_4$ film, ⟨0 0 4⟩ is the preferred orientation of growth of crystallites where as in the Eu_2O_3 doped $BaWO_4$ films, ⟨1 1 2⟩ is the preferred orientation. The XRD analysis shows that moderate doping of Eu_2O_3 increases the crystallinity and 3 wt.% Eu_2O_3 doped film is more crystalline than other films. SEM analysis reveals that the films with Eu_2O_3 doping concentration 2 and 3 wt.% show better surface morphology and grain distribution compared to other films. AFM analysis shows that all the doped films show high values of rms surface roughness. The band gap energy variation in the Eu_2O_3 doped $BaWO_4$ films is not in accordance with B–M shift and the band gap energy in the doped films is less compared to that of the undoped film. The enhanced intensity and sharpness of different Raman modes in the Raman spectrum of 3 wt.% Eu_2O_3 doped $BaWO_4$ film supports earlier inference drawn from the XRD data that BWEu-3 film is more crystalline than other films. The films with higher Eu doping concentrations (≥2 wt.%) show a PL emission peak centered around 614 nm when excited at 394 nm and may be due to the $^5D_0 \rightarrow {}^7F_2$ (0–2) transition of Eu^{3+} ion.

Acknowledgements

The author Venugopalan Pillai N. is grateful to University Grant Commission Government of India, for providing a teacher fellowship under faculty improvement programme

Authors wish to thank UGC-DAE CSR, Indore for providing various facilities.

References

[1] V. Nagirnyi, E. Feldbach, L.J. onsson, M. Kirm, A.L. ushchik, C. Lushchik, L.L. Nagornaya, V.D. Ryzhikov, F. Savikhiu, G. Svensson, I.A. Tupitsina, Radiat. Meas. 29 (1998) 247.
[2] G.R. Choppin, D.R. Peterman, Coord. Chem. Rev. 174 (1998) 283.
[3] S. Lis, M.E. Lbanowski, B.M. Akowska, Z.H. Natejko, J. Photochem. Photobiol. A 150 (2002) 233.
[4] A. Patra, D. Kundu, D. Ganguli, Mater. Lett. 32 (1997) 43.
[5] S.L. Porto, E. Longo, P.S. Pizani, L.G.P. Lima, J.M. Ferreira, L.E.B. Soledada, J.W.M. Espinoza, M.R. Cassia-Santos, M.A. Maurera, C.A. Paskocimas, I.M.G. Santos, A.G. Souza, J. Solid State Chem. 181 (2008) 1876.
[6] S. Shi, J. Gao, J. Zhou, Opt. Mater. 30 (2008) 1616.
[7] R. Manalert, M.N. Rahaman, J. Mater. Sci. 31 (1996) 3453.
[8] E. Comini, A. Toncelli, M. Tonelli, E. Zannoni, E. Cavalli, A. Speghini, M. Bettinelli, J. Opt. Soc. Am. B 14 (1997) 1938.
[9] J.T. Vega-Duran, O. Barbosa-Garcia, L.A. Diaz-Torres, M.A. Meneses-Nava, D.S. Sumida, Appl. Phys. Lett. 76 (2000) 2032.
[10] W. Strek, A. Bednarkiewicz, P.J. Dere'n, J. Lumin. 92 (2001) 229.
[11] A. Nosenko, L. Kostyk, L. Koslovs'ka, J. Lumin. 90 (2000) 49.
[12] Y.R. Do, Y.D. Huh, J. Electrochem. Soc. 147 (2000) 4385.
[13] F. Shi, J.M. eng, Y. Ren, Q. Su, J. Phys. Chem. Solids 59 (1998) 105.
[14] N.V. Kuleshov, A.A.L. Agatsky, A.V. Podlipensky, V.P.M. Ikhailov, G. Huber, Opt. Lett. 22 (1997) 1317.
[15] Y. Urata, T. Fukuda, H. Ito, S. Wada, Jpn. J. Appl. Phys. 40 (2001) 6453.
[16] Z. Song, J. Ma, X. Li, Y. Sun, J. Fang, Z. Liu, C. Gao, J. Am. Ceram. Soc. 92 (2009) 1354.
[17] A.W. Sleight, Acta Crystallogr. B 28 (1972) 2899.
[18] D.B. Cullity, Elements of X-ray Diffraction, Addison-Wesley Inc., Massachusetts, 1956.
[19] G.K. Williamson, W.H. Hall, Acta Metall. 1 (1953) 22.
[20] I. Horcas, J.M. Fernandez, J. Gomez-Roderiguez, J. Colchero, J. Gomez-Herrero, A.M. Baro, Rev. Sci. Instrum. 78 (2007) 013705.
[21] K.V. Madhuri, B.S. Naidu, O.M. Hussain, Mater. Chem. Phys. 77 (22) (2003).
[22] J. Tauc, Amorphous and Liquid Semiconductors, Plenum, London, 1974, p. 159.
[23] D.L. Wood, J. Tauc, Phys. Rev. B 5 (1972) 3144.
[24] J.R. Rani, V.P. Mahadevan Pillai, R.S. Ajimsha, M.K. Jayaraj, R.S. Jayasree, J. Appl. Phys. 100 (2006) 014302.
[25] F.M. Pontes, M.A. Maurera, A.G. Souza, E. Longo, E.R. Leite, R. Magnani, M.A.E.C. Machando, P.S. Pizani, J.A. Varela, J. Eur. Ceram. Soc. 23 (2003) 3001.
[26] S.K. Arora, B. Chudasama, Cryst. Res. Technol. 41 (11) (2006) 1089.
[27] R. Lacomba-Perales, J. Ruiz-Fuertes, D. Errandonea, D. Martínezarcía, A. Segura, EPL 83 (2008) 37002.
[28] W.G. Fateley, F.R. Dollish, N.T. Mc Devitt, F.F. Bently, Infrared and Raman Selection Rules for Molecular and Lattice Vibration, Wiley-Interscience John Wiley and Sons, Inc., New York, London, ISBN 0-471r-r25620-1972.
[29] N. Weinstock, H. Schulze, A. Müller, J. Chem. Phys. 59 (1973) 5063.
[30] M. Liegeois-Duyckaerts, P. Tarte, Spectrochim. Acta Part A 28 (1972) 2037.
[31] Kyu-Seog Hwang, Young-Sun Jeon, Seung Hwangbo, Jin-Tae Kim, Opt. Appl. 39 (2009) 375.
[32] B. Antic, J. Rogan, A. Kremenovic, A.S. Nikolic, M. Vucinic-Vasic, D.K. Bozanic, G.F. Goya, P. Colomban, Nanotechnology 21 (2010) 245702.
[33] G.S.R. Raju, H.C. Jung, J.Y. Park, B.K. Moon, R. Balakrishnaiah, J.H. Jeong, J.H. Kim, Sens. Actuators B: Chem. (2010) 395.